

Direct Simulation of Internal Flow Transient Liquid Crystal Experiments

Peter Forsyth*, Matthew McGilvray†, David Gillespie‡ and Robert Pearce§
University of Oxford, Oxford, United Kingdom, OX1 3PJ

Transient liquid crystal experiments can provide high fidelity heat transfer data for complex geometries, particularly for internal geometries where IR cameras cannot be applied. However, one main drawback of applying the technique to internal geometries is the accurate definition of the driving gas temperature and the need to define it locally in the streamwise direction. Additionally, due to transient changes in the driving gas streamwise profile, the comparison to steady state CFD has been questioned. This paper explores simulating the transient behaviour of the experiment directly. A novel technique to account for differences in the applicable time scales is developed, where the solid surface temperature is calculated analytically using the impulse response method for a semi-infinite conduction and coupled to CFD solver directly. This is compared to the application of transient conjugate heat transfer. Both numerical methods are applied to simulate a transient liquid crystal experiment of a stationary super-scaled rib turbulated internal cooling passage. The surface temperature from the numerical results is post-processed using the method applied in the experiment to ensure direct comparison. Results show that calculations using the new analytical method and steady state gave very similar Nusselt number distributions and mean value in relation to the experimental data. Analysis of transient variation of Nusselt number indicated localised maximum variations up to 40%, though this was not found to significantly effect the minimised global values.

Nomenclature

Symbols	Subscripts
A = Area, [m ²]	g = Gas
Bi = Biot number, $\frac{lh}{k_r}$	i = Initial
c_p = Specific heat capacity at constant pressure, [J/(kg.K)]	0 = Reference
D_h = Hydraulic diameter, [m]	fp = Flat plate
e = Rib height, [m]	p = Projected
f = Friction factor, $\Delta P \frac{D_h}{2\rho V^2 L}$	r = Rib
H = Passage height, [m]	s = Surface
h = Heat transfer coefficient, [W/(m ² .K)]	Greek
k = Thermal conductivity, [W/(m.K)]	α = Rib angle, [°]
l = Characteristic length	β = Equation 7
m = Mass [kg]	θ = Non-dimensional surface temperature
Nu = Nusselt number, $\frac{h.l}{k}$	λ = Direction of curvature
p = Rib pitch, [m]	μ = Viscosity, [Pa.s]
P = Pressure, [Pa]	ρ = Density, [kg/m ³]
P = Perimeter [m]	Abbreviations
\dot{q} = Heat flux, [W/m ²]	ABC = Analytic boundary condition
r = Radius, [m]	AR = Aspect ratio, (W/H)
Re = Reynolds number, $\frac{\rho.v.l}{\mu}$	ERICKA = Engine Realistic Internal Cooling Knowledge Applications
T = Temperature, [K]	HTC = Heat transfer coefficient
t = Time, [s]	LE = Leading edge
v = Velocity, [m/s]	PS = Pressure side
W = Passage width, [m]	SS = Suction side
z = Material depth, [m]	TCHT = Transient conjugate heat transfer
	TE = Trailing edge

*Research Assistant, Department of Engineering Sciences, Parks Rd Oxford, peter.forsyth@eng.ox.ac.uk

†Associate Professor, Department of Engineering Sciences, Parks Rd Oxford, matthew.mcgilvray@eng.ox.ac.uk

‡Associate Professor, Department of Engineering Sciences, Parks Rd Oxford, david.gillespie@eng.ox.ac.uk

§Research Assistant, Department of Engineering Sciences, Parks Rd Oxford, robert.pearce@eng.ox.ac.uk

I. Introduction

Measurement of the heat flux on complex surfaces is difficult, particularly for internal geometries found in gas turbine engines. Transient heat transfer experiments measure the distribution of heat transfer coefficient by measuring both the driving gas temperature and surface temperature response, typically for a near-step change in the gas temperature [1]. The resulting heat flux causes a change in the surface temperature. As the experiment is initially at isothermal conditions and the solid is thick enough to ensure semi-infinite conduction, the Fourier heat conduction equation can then be solved to determine the heat transfer coefficient. Post-processing of the raw data can be undertaken using a variety of techniques from finite difference, analytical derivations [2] to the impulse response method [3]. Corrections for complex geometry exist [4,5] and application of transient FEA can even be applied to truly 3D geometries [6,7].

For thermochromic liquid crystal (TLC) experiments, surface temperature information comes from imaging thermochromic liquid crystals sprayed onto the target surface [2]. The helical structure of the crystals alters the reflected wavelength of light depending on the temperature (*i.e.* the surface changes colour with temperature). Although improvements in IR camera technology has seen a reduction in TLC's application for external flow cases, the difficulties for imaging the internal surface has seen a continued application of the method. Narrow band liquid crystals have been shown to produce the most robust and accurate solutions, particularly if multiple crystals are applied to give information over a wide range of temperatures [8]. The technique is widely used for measuring heat transfer from gas turbine internal cooling component geometries. For stationary testing, it is common to use an increase in the gas temperature via a fast acting valve system or a heater mesh.

Differences in heat transfer coefficient between transient experiments and steady state experiments/CFD, independent of the uncertainties in the experiment, are widely attributed to the following:

- the definition of driving gas temperature
- gas temperature transients over the course of the experiment
- an approximation of one-dimensional conduction
- establishment of the thermal boundary layer
- changing hydrodynamic conditions in the system

One difficulty for measuring internal flow heat transfer coefficients using transient TLC is the definition of the driving temperature. For any slice of gas as it convects downstream will drop in temperature due to thermal energy lost to the solid. As the solid heats up with time, the amount of thermal energy lost to the solid as the slice of gas convects down the passage decreases. This is in contrast to external flows where a single driving gas temperature history can be applied. Also, the change in gas temperature is never truly a step change.

To overcome this, experimentalists exhibit extreme care in the use of either convolution strategies (e.g. [3]) or time delayed series solutions of simple gas temperature input profiles to model the substrate behaviour fully during a test. For example: in [9] the local temperature distribution during start-up is not used to determine the HTC, allowing its application in test rigs where there may be transient compression of incoming test gas. In most transient liquid crystal tests a test strategy is used with many fast response thermocouples providing a good description of the spatial and temporal gas temperature distribution and this is used to model the system as a series of steps, ramps [2] or exponential rises in gas temperature [10]. Many experimentalists use the full colour range of wide band crystals [11], or the non-dimensionalised intensity history [12] to introduce redundancy into the solution of the system of equations.

The spatially resolved driving gas temperature is defined in one of two ways. First a local temporally varying driving gas temperature may be prescribed, typically by interpolation of thermocouples in the domain or by an energy balance along a passage. Where there is sufficient redundancy in the data the local adiabatic wall temperature may be determined, which is particularly useful for 3 temperature problems, but it must be noted that this may or may not be similar to any defined bulk temperature.

The significance of 3-D conduction effects can be assessed by post processing of the 1-D results to determine a pseudo value of

$$\frac{\partial^2 q}{\partial y^2} \ll \frac{\rho c_p}{k} \frac{q}{2t} \quad \text{and} \quad \frac{\partial^2 q}{\partial z^2} \ll \frac{\rho c_p}{k}, \quad (1)$$

where y and z are spanwise and axial directions in a local coordinate frame. Approaches such as the 3-D ADI method have been used to correct the output from the 1-D solution [5], and corner corrections [4] or full 3-D analyses have also been employed ([7]).

Another consideration is what effect does the transient change in the thermal boundary layer has on the local heat transfer coefficient, which in a transient TLC experiment will be continually changing. Cukurel and Arts [13]

demonstrated this is significant by comparing two steady state cases of an iso-heat flux and a convective boundary condition. This has led to strategies applying three point non-linear corrections when applying steady state CFD to determine local heat transfer coefficients [14].

Even with this body of work, the comparison between HTC values derived from transient experiments and steady-state CFD is still questioned. A well intentioned paper by Sathyanarayanan and Shih [15] reports differences between HTC determined from carefully conducted transient conjugate CFD simulations, using techniques they believed to be representative of best experimental practice. Disappointingly in light of the very many publications on the transient heat transfer techniques, there are numerous simplistic assumptions made as to typical means of data reduction, and sadly the conclusions drawn are highly misleading. Their reported variance of 30% in HTC will be shown to be a large over-prediction.

This paper will detail the novel application of a quasi-transient technique for simulating the experiment to provide the same definition of gas temperature. It uses CFD to solve the fluid and the heat flux distribution, with the surface temperature calculated analytically applying the impulse response method. The method will then be applied and compared to a TLC experiment of a rib roughened passage [16]. This will be compared to transient conjugate heat transfer of the same test and steady state CFD. This paper also redresses some of the conclusions drawn in [15] and provides a true assessment of HTC values determined by steady state CFD in comparison to HTC values determined from experimental transient liquid crystal testing in a rib turbulated passage.

II. Stationary Internal Cooling Passage Experiments

The experimental data simulated in this paper is from an aspect ratio 1:3 super-scaled rib roughened internal cooling passage. The geometry is typical to that found in modern gas turbine engines. The experiment applied the TLC technique using a 25, 30 and 35 °C narrow band liquid crystal mixture. The gas temperature was measured on the centreline at five locations, TC1 (upstream) - TC5 (downstream). The flow was stabilised at atmospheric pressure and ambient temperature, isothermal with the perspex walls. The mass flow rate was measured using British Standard orifice plate arrangement upstream of the passage. The experiment used a heater mesh upstream to rapidly heat the flow, from ambient conditions. The passage is made from Perspex, which has a thermal product of $569 \text{ W/m}^2\text{s}^{0.5}\text{K}$ and is thick enough over the 30 second test time for the external surface to remain isothermal. A detailed description of the setup of the experiment can be found in [17, 18].

A. Geometry

The internal cooling passage test section consists of a 432 mm long filleted rectangular duct with rib turbulators on two opposing walls (suction and pressure surface). The remaining walls (leading and trailing edge) are smooth, as seen in Figure 1. Ribs in the passage are: at an angle (α) of 45° to the streamwise direction; a pitch to height spacing (P/e) of 10; filleted along all edges (radius of filleting is $e/2$); centred in the passage; span half the width of the passage; staggered by half the pitch between the suction and pressure surface; have a 0.9 mm base which is fully recessed into the passage wall; are made of brass. Both ribbed walls have 24 ribs. The passage has an aspect ratio (width:height) of 1:3 with a rib blockage (e/D_h) of 6.2% and a hydraulic diameter of 29.0 mm. The passage width is 18.66 mm. The rig can be reconfigured to allow HTC data to be collected on all four walls.

The data from each surface is transformed using a linear interpolation to account for non-linearity in radial geometry and rotation, then combined to form a single map (Figure 1c). Where there is an overlap between images, the data is cropped to the midpoint of the passage fillet for recombination. This minimises the area scaling applied to individual pixels. Each wall is appropriately rotated to reflect the layout of the experimental passage.

B. Flow Conditions

The baseline flow condition was initially stabilised under isothermal conditions and a constant axial pressure difference at the target mass flow rate. During the experimental the constant pressure difference was maintained, which drives a constant volume flow rate through the test section. The mass flow rate and Reynolds number therefore vary as the gas temperature changes. Under these boundary conditions, the rising gas temperature caused the mass flow rate and passage Reynolds number to fall over the experimental time by 7.1 %. Reynolds numbers reported were based on the most downstream centreline gas thermocouple, TC5.

III. Numerical Methodologies

The problem is approached with three different methods: (A) a quasi-transient modelling the fluid domain in CFD with the solid surface temperature analytically calculated using the impulse response method for a semi-infinite solid,

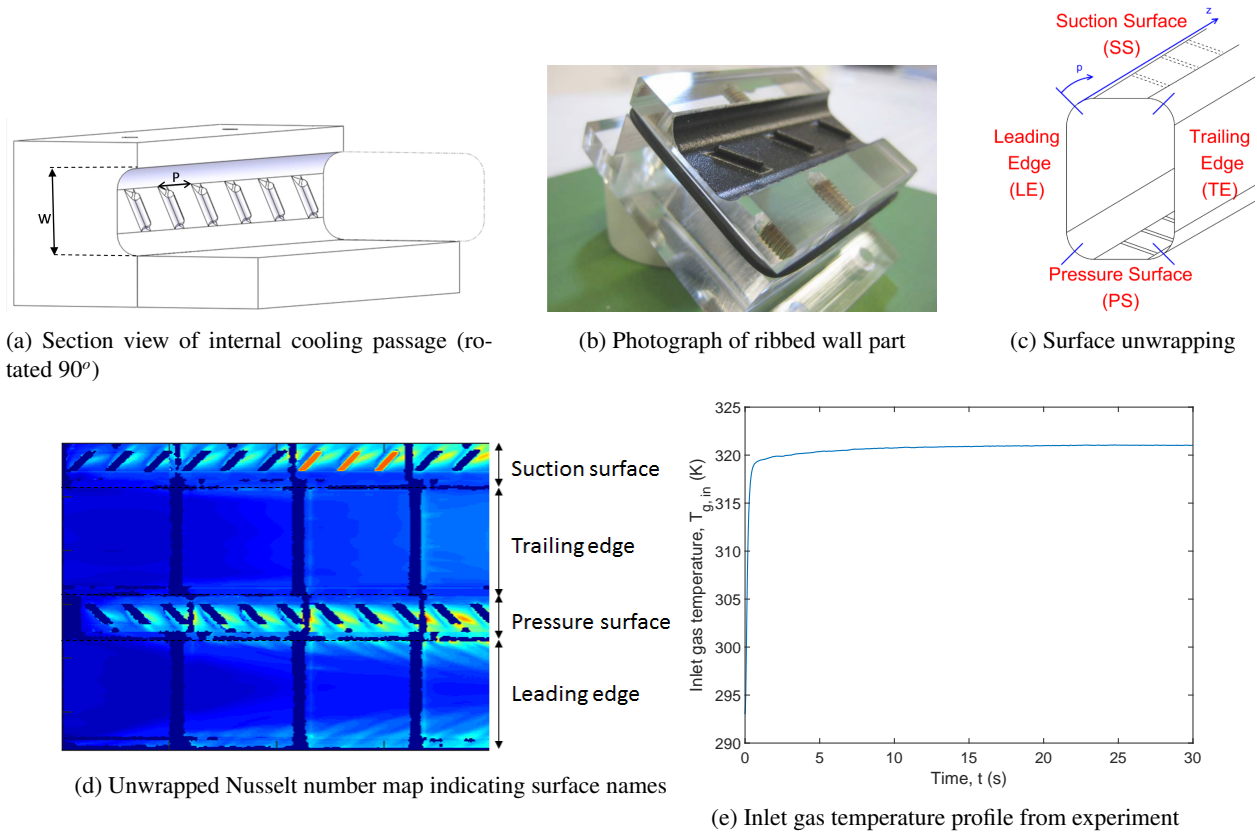


Figure 1: Experimental passage geometry, surface naming convention, and inlet gas temperature profile as applied in simulations

(B) fully transient conjugate heat transfer, (C) steady state CFD with constant fixed wall temperature.

All three methodologies employed the unwrapping technique used experimentally, Figure 1c, in order to map the curved surfaces to a linear plot for comparison to the experimental data. Where normalised Nusselt number data is presented, the normalising value is the fully-developed turbulent pipe flow Nusselt number, given by

$$Nu_0 = 0.023Re^{0.8}Pr^{0.4}, \quad (2)$$

where Re is the bulk Reynolds number based on ribbed channel hydraulic diameter, and Pr the Prantl number. Area-averaged comparisons to the experimental data are made over the downstream half of the passage (ribs 13-24), following [17]. Pixels where the experimental processing failed, marked 'not a number' (NaN) by MATLAB, are excluded from averaging. The experimental mean normalised Nusselt number values were recalculated for this paper.

A. Analytic Boundary Condition

The quasi-transient analytic boundary condition (ABC) simulations apply the assumption of semi-infinite 1D heat conduction made experimentally for the calculation of heat transfer coefficients. This method is analogous to that of He and Oldfield [19] for fluctuating flows generated by blade passing events. As the time scales related to the transient fluid flow are extremely small ($t \approx 5 \times 10^{-4}$ s, based on bulk velocity and hydraulic diameter) in comparison to those related to transient heat conduction in the solid (75 s for the thermal pulse to reach the outside boundary of the test section, [1]), there is a large computational cost in accurately simulating the transient nature of the flow with the transient conduction in the solid. Due to this disparity in time scales, the fluid solution is considered steady at each time step.

The flow was solved using ANSYS FLUENT 18.2. The SST turbulence model was chosen. Pressure and velocity were coupled, and second order upwind spatial discretisation of gradients was used. Scaled residuals were monitored as per Section 1. The calculation of surface temperatures and heat transfer coefficients was done in two parts; this is outlined in Figure 2, are described in detail below.

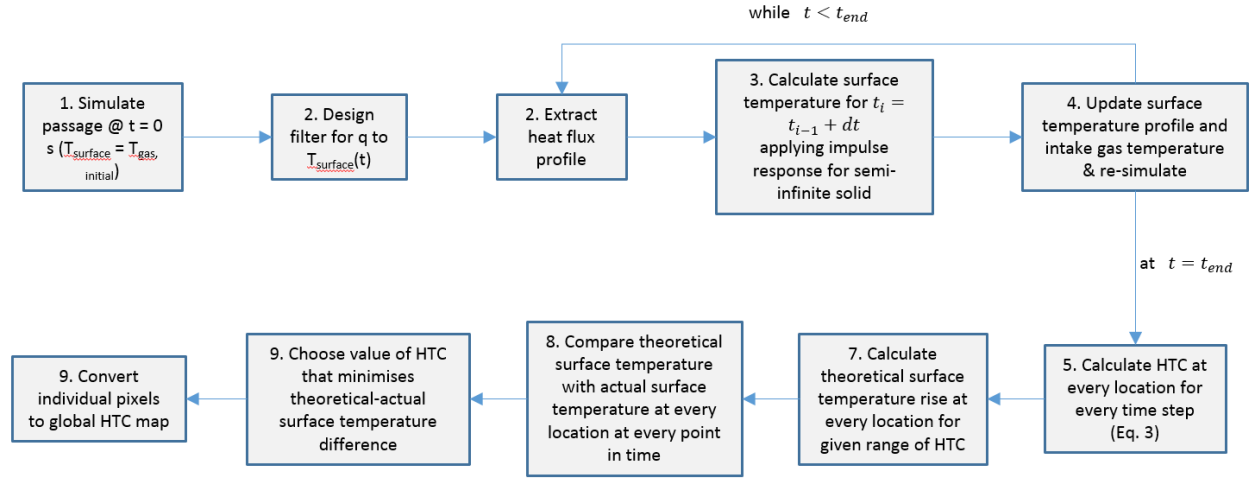


Figure 2: Flow chart of analytical boundary condition (ABC) method

1. Perspex walls: simulation

The wall temperature is calculated from the wall heat flux, using the impulse response method [3] for solution of the 1D heat equation, assuming the solid to be a semi-infinite body. The impulse response method uses convolution of an appropriate filter with the input signal (surface heat flux or temperature) to calculate the response of the surface (surface temperature or heat flux respectively).

Initially a filter H is designed by deconvolution of a $\dot{q}(t) - T_s(t)$ pair, in this case from the analytic solution of surface temperature response due to a step change in heat flux. At each time step, the surface heat flux was read into MATLAB, where the surface temperature is then calculated for the time step by filtering the time history of the surface heat flux $\dot{q}(t)$. The surface temperature profile is then written back to Fluent, where the fluid solution is reconverged.

2. Perspex walls: post-processing

The heat transfer coefficient is calculated at each location at each point in time based on the heat flux and surface temperatures from the simulation,

$$h(t, x, y, z) = \frac{\dot{q}(t, x, y, z)}{T_g(t, z) - T_s(t, x, y, z)}. \quad (3)$$

The centreline gas temperature, $T_g(t)$, is interpolated between the five axial thermocouple locations as per the experiments. To account for radial conduction in the concave filleted corners of the passage, the general curvature correction method of Buttsworth and Jones [4] was been applied,

$$\dot{q} = \dot{q}_{fp} - \frac{\lambda k}{2r} (T_s - T_i). \quad (4)$$

Here \dot{q}_{fp} is the flat plate heat flux, λ is -1 for concave cylindrical surfaces, and k the thermal conductivity of the wall (0.2 W/(m.K)). This correction is not limited to constant h .

The spatial heat transfer coefficient $h(t, x, y, z)$ may vary over the test. Similarly to the processing of the experiments simulated [16], the heat transfer coefficient at each point on the surface can be calculated. The 1D Fourier equation for a semi-infinite solid is solved in non-dimensional temperature space for a step change in driving gas temperature for a range of nominal heat transfer coefficients, h ,

$$\theta(t, 0) = 1 - \exp(\beta^2) \operatorname{erfc}(\beta). \quad (5)$$

Non-dimensional temperature θ , and β are given by

$$\theta(t, 0) = \frac{T_s(t, 0) - T_i}{T_g - T_i}. \quad (6)$$

$$\beta = \frac{h\sqrt{t}}{\sqrt{\rho ck}}, \quad (7)$$

The thermal product of the semi-infinite substrate, $\sqrt{\rho ck} = 569 \text{ W/m}^2\text{s}^{0.5}\text{K}$. Based on the gas temperature history at each spatial location and for each h , the theoretical surface temperature rise can be calculated. The global heat transfer coefficient at each spatial location is found by minimising the root sum of squares (RSS) difference between the simulated and theoretical surface temperature profiles at each point in time.

3. Hybrid brass ribs: simulation

A hybrid rib method, following Wang [20], was implemented. This approach uses a lumped thermal mass for the ribs, which leads to a uniform rib temperature and hence a uniform effective heat transfer coefficient can be calculated at the bottom (perspex wall) side of rib. During the simulation, three processes are considered at each time step: heat convected into the rib (Q_{conv}), heating of the rib (Q_{rib}), and conduction of heat into the semi-infinite substrate below via the effective heat transfer coefficient (Q_{cond}), as per Section 1. Taking an energy balance of these processes allows the rib temperature to be calculated on an iterative basis for each time step. Rib properties were: $\rho_r = 8490 \text{ kg/m}^3$, $c_{p,r} = 380 \text{ J/(kg.K)}$, $k_r = 108 \text{ W/(m.K)}$, $m_r = 0.63 \text{ g}$.

4. Hybrid brass ribs: post-processing

A solution to the 1D heat equation is used to produce theoretical surface temperature histories beneath the rib, as per the above section. This is based on a two-layer approach: a high thermal diffusivity layer on top of the low diffusivity semi-infinite substrate,

$$\theta(t, 0) = 1 - \frac{h}{\beta_r} \frac{1}{b-a} \left[\frac{1}{a} \exp(a^2 t) \operatorname{erfc}(a\sqrt{t}) - \frac{1}{b} \exp(b^2 t) \operatorname{erfc}(b\sqrt{t}) \right], \quad (8)$$

where

$$a = \frac{\sqrt{\rho ck}}{2\beta_r} - \sqrt{\left(\frac{\sqrt{\rho ck}}{2\beta_r} \right)^2 - \frac{h}{\beta_r}}, \quad (9)$$

$$b = \frac{\sqrt{\rho ck}}{2\beta_r} + \sqrt{\left(\frac{\sqrt{\rho ck}}{2\beta_r} \right)^2 - \frac{h}{\beta_r}}, \quad (10)$$

and

$$\beta_r = \rho_r c_{p,r} l_r \left(1 - \frac{h l_r}{2k_r} \right). \quad (11)$$

As the second term in Eq. 9, 10 can be complex, a complex error function must be used in Eq. 8. The global heat transfer coefficient for each rib is then found by minimising the RSS difference between the transient spatial values calculated at each simulation time step and the theoretical solution from Eq. 8, as per Section 1.

B. Transient conjugate heat transfer

The transient conjugate heat transfer (TCHT) simulations were carried out using ANSYS CFX 18.2. Three-domain grids were constructed (see section D): fluid, perspex, and brass ribs. These were done as described in Section D. The inlet gas temperature profile, Figure 1e was applied. The simulations used the SST turbulence model for the closure of the RANS equations, with the ‘high resolution’ options for advection and turbulence numerics, and the ‘Second Order Backward Euler’ scheme for time-stepping.

Surface temperature data was exported from the fluid-perspex surfaces, and the outer surface of the rib, as is seen by the camera in the experiments, along with the centreline gas temperature profile. The same methods as per Section 1 are applied to calculate a global (time-independent) HTC distribution.

C. Steady state

Steady state CFD was carried out for comparison to the ABC and TCHT solutions. These calculations were carried out using a standard industry approach: boundary conditions of a uniform fixed wall temperature for all surfaces (293 K), with an inlet total temperature of 313 K. These temperatures are representative of those used experimentally. Numerical solution (ANSYS Fluent, $k - \omega$ SST turbulence modelling) was as described for the ABC simulations above. The same mesh was used for the ABC simulations.

Processing was carried out by calculating the heat transfer coefficient with reference to the centreline gas temperature at the same axial location,

$$h(x, y, z) = \frac{\dot{q}(x, y, z)}{T_g(z) - T_w(x, y, z)}. \quad (12)$$

Rib values of heat transfer coefficient were calculated by scaling the rib-fluid heat transfer coefficient by the ratio of rib surface area to rib projected area,

$$h_r = \frac{\sum(h_{p,z}A_s)}{\sum(A_p)}, \quad (13)$$

where the summations are carried out over each face cell of a rib. The ratio of rib surface area A_s to rib projected area A_p was 1.49. Gas temperature was calculated from interpolation of the five gas temperature measurement locations as above. Viscosity was calculated using Sutherland's law, using the interpolated gas temperature at each spatial location.

D. Mesh generation and grid independence

Mesh generation was carried out using ANSYS ICEM 15.0. Unstructured meshes were generated from tetrahedral cells, with prism layers grown on the all wall surfaces. Initial cell heights were: rib = 0.03 mm, pressure/suction surfaces = 0.05 mm, other walls 0.08 mm, which were found to give $y^+ < 1$ across the domain, and were kept constant across all meshes. These parameters were also applied to generate prism layers within the two solid perspex region for TCHT grids. Within the ribs the parameters were reduced to initial cell height (0.02 mm), number of layers (8) and the expansion ratio (1.1) to improve mesh quality due to tight angles.

Four grids were generated, 3.11-12.9 M cells were generated. Steady state calculations were run as per Section C: $T_{g,in} = 313$ K, $\dot{m}_{g,in} = 40$ g/s, $T_w = 293$ K. Total heat transfer rate through the pressure and suction surfaces \dot{Q}_{PS+SS} , and mass-averaged static temperature \bar{T}_e were the assessed variables; these are summarised in Table 1. It is seen that the convergence for \bar{T}_e is extremely close, with the coarse mesh being < 0.2 % from the very fine grid. The convergence of \dot{Q}_{PS+SS} was less strong, but the coarse mesh was deemed to be adequate here too (0.8 % absolute difference to the very fine mesh). Based on this assessment, the coarse mesh was used throughout the ABC.

Analysis of the TCHT simulations indicated that a finer grid was required. The same parameters were applied as for the ABC grid, but the scale factor reduced. The chosen TCHT grid had 10.66 M cells.

Grid	No. cells (M)	Prism layer	\dot{Q}_{PS+SS} (W)	Diff. to v. fine (%)	\bar{T}_e (K)	Diff. to v. fine (%)
Coarse	3.11	$N = 8, r_e = 1.6$	37.4	0.80	305.4	0.13
Medium	5.38	$N = 15, r_e = 1.3$	36.9	2.11	304.7	0.10
Fine	9.52	$N = 15, r_e = 1.3$	38.0	0.80	304.91	0.03
V. fine	12.9	$N = 15, r_e = 1.3$	37.7	-	305.0	-

Table 1: Mesh independence study reporting percentage difference to very (v.) fine grid. \dot{Q}_{PS+SS} : heat transfer rate through pressure and suction sides (W). \bar{T}_e : mass-averaged gas temperature at domain exit (K).

E. Solution Sensitivities

1. Scaled residual convergence

Simulation time is heavily dependent on the convergence criteria set. The dependence of the solution on the criteria for scaled residual convergence was investigated using a steady state calculation. The total convective heat flux \dot{q} was

measured at five different convergence limits, Table 2, and compared to the fully converged solution (case 4). The percentage difference in \dot{q} is shown in the final column. Based on this investigation, the case 2 convergence limits were used throughout.

Case	Continuity	x, y, z -velocity	k, ω	Energy	Iterations	\dot{q} relative diff. (case 4)
1	10^{-3}	10^{-3}	10^{-3}	10^{-6}	90	1.4%
2	5×10^{-4}	10^{-6}	5×10^{-5}	10^{-6}	280	0.22%
3	5×10^{-4}	10^{-6}	10^{-5}	10^{-6}	500	0.016%
4	1.1×10^{-4}	10^{-6}	6×10^{-6}	10^{-6}	1000	-

Table 2: Scaled residual criteria with absolute percentage difference in convective heat flux \dot{q} from domain, relative to fully converged case (4)

2. Time step

ABC simulations were carried out using a range of constant time steps: 0.01, 0.025, 0.05, 0.1 s. These simulations were carried out for 1.0 s, which accounts for 94.3% of the inlet gas temperature rise. Simulations were carried out at $Re = 60,000$, using the computational methods described in Section A.

Area-averaged comparisons of Nusselt number distributions indicated that in relation to the 0.01 s time step, the 0.1, 0.05, 0.025 s simulations had a mean absolute difference of 2.8, 0.9, 0.3% respectively, Figure 3a. The displayed values are sampled at the lowest frequency trialled (10 Hz). Comparisons of the surface temperature rise on the 20th rib and leading edge, Figure 3b. As the simulation progresses in time, the difference in surface temperature between the varying time steps reduces: a maximum difference of 0.8 K is seen at $t = 0.2$ s, whereas by $t = 1.0$ s, the maximum difference was 0.1 K. Relative to the 0.01 s time step, the 0.1, 0.05, 0.025 s simulations were lower by 0.29, 0.11, 0.04%. Based on these assessments, the 0.025 s time step (40 Hz) was therefore chosen, and applied to both the ABC and TCHT simulations.

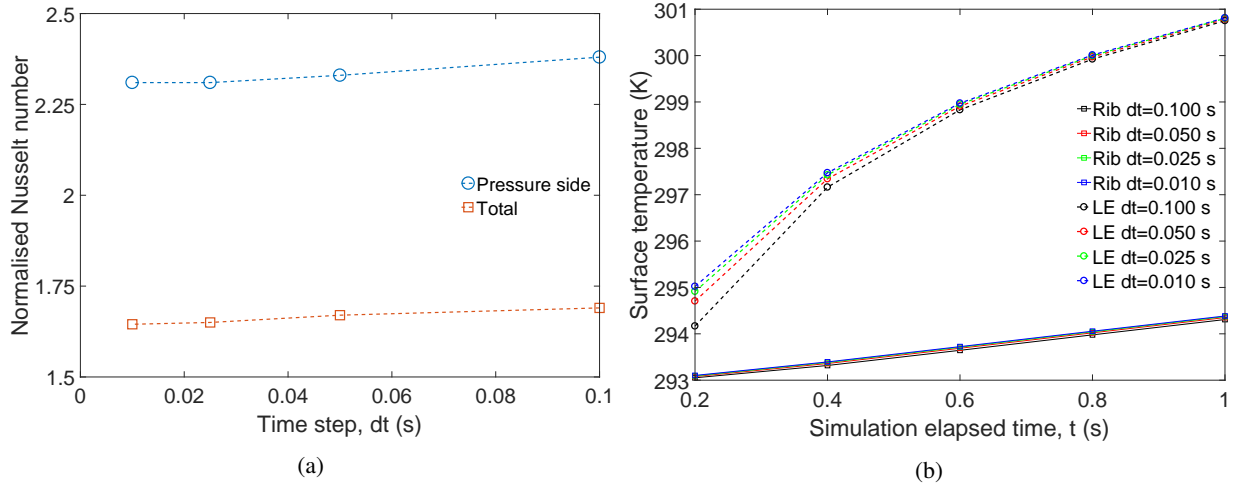


Figure 3: Summary of investigation into effect of time step on quasi-transient simulations. (a) Area-averaged normalised Nusselt number on pressure side and total area. (b) Surface temperature rise on 20th rib and leading edge.

IV. Results

The conditions simulated in this paper have a passage Reynolds number of 60,000 based on hydraulic diameter, and pressure inlet and outlet conditions to target a mass flow rate (40 g/s). The initial isothermal temperature was 293 K, with the transient temperature inlet profile extracted experimental thermocouple data, Figure 1e. The pressure in the experiment is 1 bar.

A. Mass flow rate and Reynolds number

The variation of mass flow rate and Reynolds number with time is shown in Figure 4. The simulation mass flow rate profile with time qualitatively falls as the experimental mass flow rate was seen to, however the decrease in mass flow rate is 3.9% in comparison to 1.1% seen in the simulation. The Reynolds number shows the opposing trend, simulation falls 4.0% in comparison to experimental 7.1%. This is switch is due to differing values of μ_g due to different gas temperatures simulated relative to the experimental work.

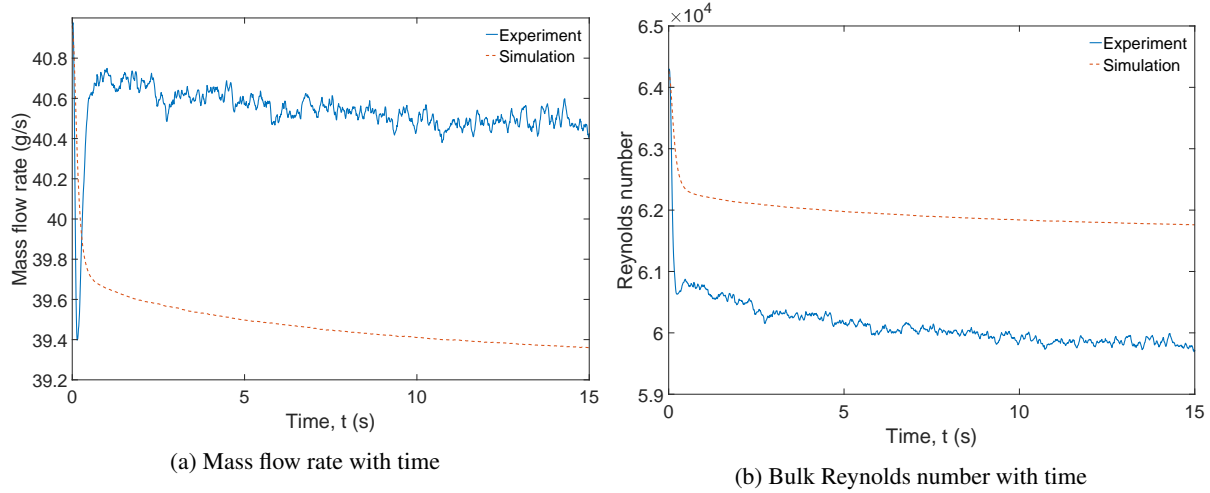


Figure 4: Variation of mass flow rate and Reynolds with time

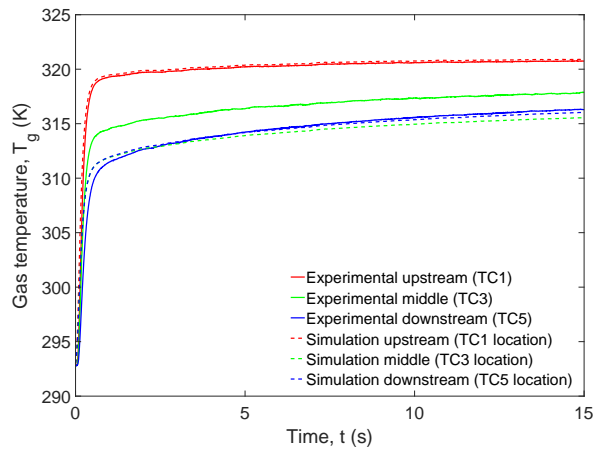
B. Gas temperature profiles

Figure 5 shows comparisons between experimental and simulated gas temperature profiles. Figure 5a shows pointwise gas temperature profiles with time, for thermocouples different axial locations: start (TC1), $z = 12.5$ mm; middle (TC3), $z = 226$ mm; end (TC5), $z = 422$ mm. Axial position $z = 0$ mm corresponds to first rib location. For the TC1 and TC5 locations, the simulation is able to well-predict the experimental temperature. A small disparity (8.4 % of temperature difference $T_{g5} - T_i$) is seen in the TC5 trace in the first second, indicating the transient behaviour is not fully captured. The middle thermocouple, TC3, is not well simulated. The reason for this can be seen in the streamwise gas temperature comparisons, Figure 5b. Here it is observed that the simulations predict a ‘trough’ in gas temperature in the middle region axially of the passage ($z = 150 - 220$ mm), followed by a recovery ($z = 220 - 400$) mm. The presence of this trough and recovery is a phenomenon seen experimentally, with its exact streamwise location being highly influential on the interpolated gas temperature profile. It is noted that the transient conjugate heat transfer profile (green) shows a significantly downstream trough in comparison to the experimental, analytic boundary condition, or steady state simulations. This is thought to be a key driver for the differences noted in spatial Nusselt number distributions that follow. Interpolated gas temperature profiles, taken at the experimental thermocouple locations, are seen in Figure 5c.

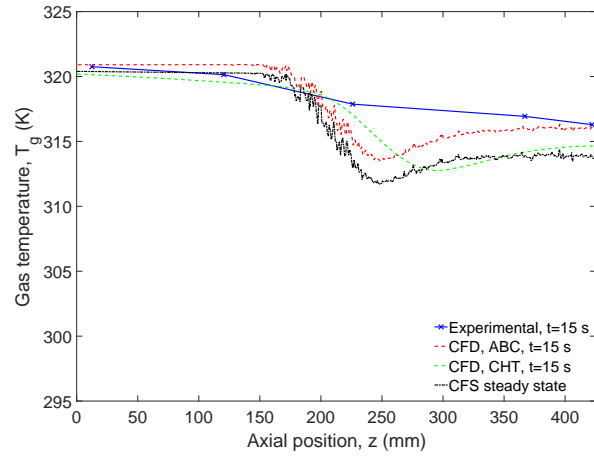
Whilst the streamwise profiles show that the temperature recovery location is highly influential, the profiles indicate that the quasi-transient simulations are able to capture changing centreline gas temperature with time. As the simulation progresses, it is observed that the profiles become more uniform: the ABC simulation captures the transient heating of the passage walls, leading to a smaller fall in centreline gas temperature down the passage in the later stages of the simulation. The centreline gas temperature as used in the steady-state simulations is also shown. It is observed that this is less representative of the gas temperature profile at the end of the experiments in comparison to the ABC simulations as this transfer of heat from gas to wall has not been accounted for.

C. Surface heat flux and temperature distributions

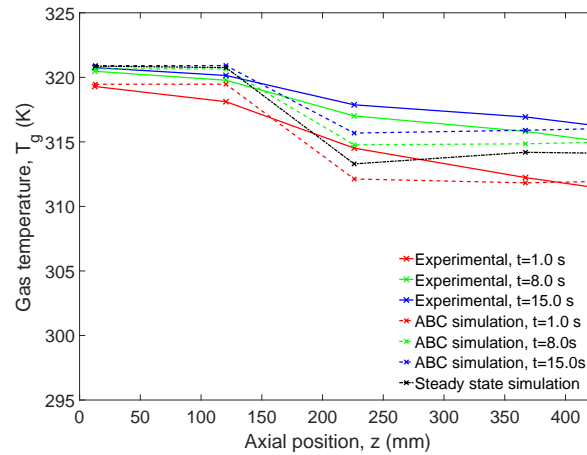
Plots of spatial surface heat flux \dot{q} and surface temperature T_s for the analytic boundary condition and transient conjugate heat transfer are shown in Figure 6. In the analytic boundary condition simulations, the heat flux distribution is read from the simulation at every time step, and the surface temperature rise calculated by impulse response. This can be seen to change substantially during the simulation period (shown at $t = 1.0, 15.0$ s.) The rib values can be seen



(a) Thermocouple location histories



(b) Linearly extrapolated streamwise distribution



(c) Linearly extrapolated streamwise distribution

Figure 5: Comparison of centreline gas temperature between the experiment and quasi-steady simulation.

to be lower than the surrounding perspex surfaces, due to their low Biot number ($Bi < 0.1$) heating the rib uniformly, hence slower than the surface of the semi-infinite substrate.

D. Nusselt number distributions

1. Spatially-resolved

Nusselt number distributions for the analytic boundary condition, transient conjugate heat transfer, and steady state simulations are shown against the experimental data in Figure 7. The bulk flow Reynolds number was 60,000. Surface names (suction side, trailing edge, pressure side, leading edge) are as Figure 1d. As no experimental rib values are available for the suction side, this surface is excluded from the following discussion.

The ABC simulation, Figure 7b is observed to be a reasonable match to the experimental data. The pixel-wise mean absolute difference was found to be 21.6% across the downstream half of the map ($z > 220$ mm). The mean difference in area-averaged Nusselt number was 8.6% below experimental. On the pressure surface, the mean absolute difference to experimental rib Nusselt number values was 6.4%, with the trend, peaking ribs 12-17, then falling, well captured.

The TCHT simulation, Figure 7c, did not reproduce the experimental data as closely. The pixel-wise absolute mean difference was 29.2%, with a area-averaged difference of 40% below the experimental value. Whilst the trailing edge impingement region is well-matched to the experimental level, the area-averaged level is 36.5% below the experimental. The ribbed surface heat transfer mean absolute difference of 40.6% to the experimental is noted, and qualitatively the peak rib values are seen further downstream than experimentally. This is thought to be related to the TCHT simulations not capturing the trough/fall and recovery of centreline gas temperature location correctly.

The steady state simulation results, Figure 7d, is observed to be extremely similar to the ABC distribution. The pixel-wise mean absolute difference was 20.5%, with an area-averaged difference of 7.1% below experimental levels, both closer to the experimental data than the ABC simulations. The rib levels were less well predicted than the ABC method, 6.6% difference.

These results show that the steady state and quasi transient method give very similar Nusselt number distributions. From this we see that any variation in HTC and hence Nusselt number with time using the quasi transient method is negligible when the final distribution is calculated.

2. Variation of Nusselt number with time

Following the discussion in [15] regarding the variation of heat transfer coefficient with time during a transient test, Figure 8 plots axial profiles of Nusselt number with time. The underlying HTC maps are constructed using Eq. 3. Two locations are used: in the middle of the pressure surface ($p = 80$ mm) and the middle of the trailing edge ($p = 45$ mm). Both locations are shown as absolute Nusselt number (plots (a) and (c)), and as percentage difference to final value Nusselt number at $t = 15.0$ s, given as a percentage (plots (b) and (d)), $(Nu(t) - Nu_{t=15.0s}) / Nu_{t=15.0s}$. The rib values, flat regions in (a) and (b), should be disregarded as the hybrid rib processing is carried out after this point in the method.

A number of interesting features are seen. The Nusselt number distribution is seen to vary somewhat with time on both the pressure side and trailing edge. On the pressure surface, Figures 8a and 8b, the variation is largest in the developing region of the passage, $z < 220$ mm. This is seen to be up to 43% at $t = 1.0$ s relative to $t = 15.0$ s. By $t = 5.0$ s the maximum difference is seen to fall to 18%. In the region of the passage where the secondary flow vortices are seen to coalesce and impinge the trailing edge ($250 < z < 310$ mm, see Figure 7b and discussion in [8]), the variation of Nu with time is significantly lower, peaking at 12% difference, and quickly converging to $< 5\%$ difference. This is potentially due to the better mixing of the flow in this region. Moving downstream, $z > 310$ mm, the variation with time increases to a maximum of 21% at $t = 1.0$ s, and 8% by $t = 5.0$ s.

On the trailing edge, the variation of Nusselt number with time is significantly lower. This is clearly seen from Figure 8c. Peak values of 12% are seen in the early developing flow region ($z < 10$ mm), however convergence towards a steady value is rapid for most of the passage: for $z > 25$ mm, by $t = 5.0$ s all of the passage is below 2.5% difference to the $t = 15.0$ s solution.

Area-averaging the Nusselt number at every time step was carried out. It was observed that the transients have a small effect on the mean value; the area-averaged value converged to within 0.5% of its steady value within 0.2 s. It was also observed that the global minimisation process applied to match simulated surface temperature against theoretical surface temperature from Eq. 5, given a range of h , is not significantly affected by the transient variation of spatial HTC or Nu . Whilst this transient behaviour is noted, it is not significantly affecting the global results.

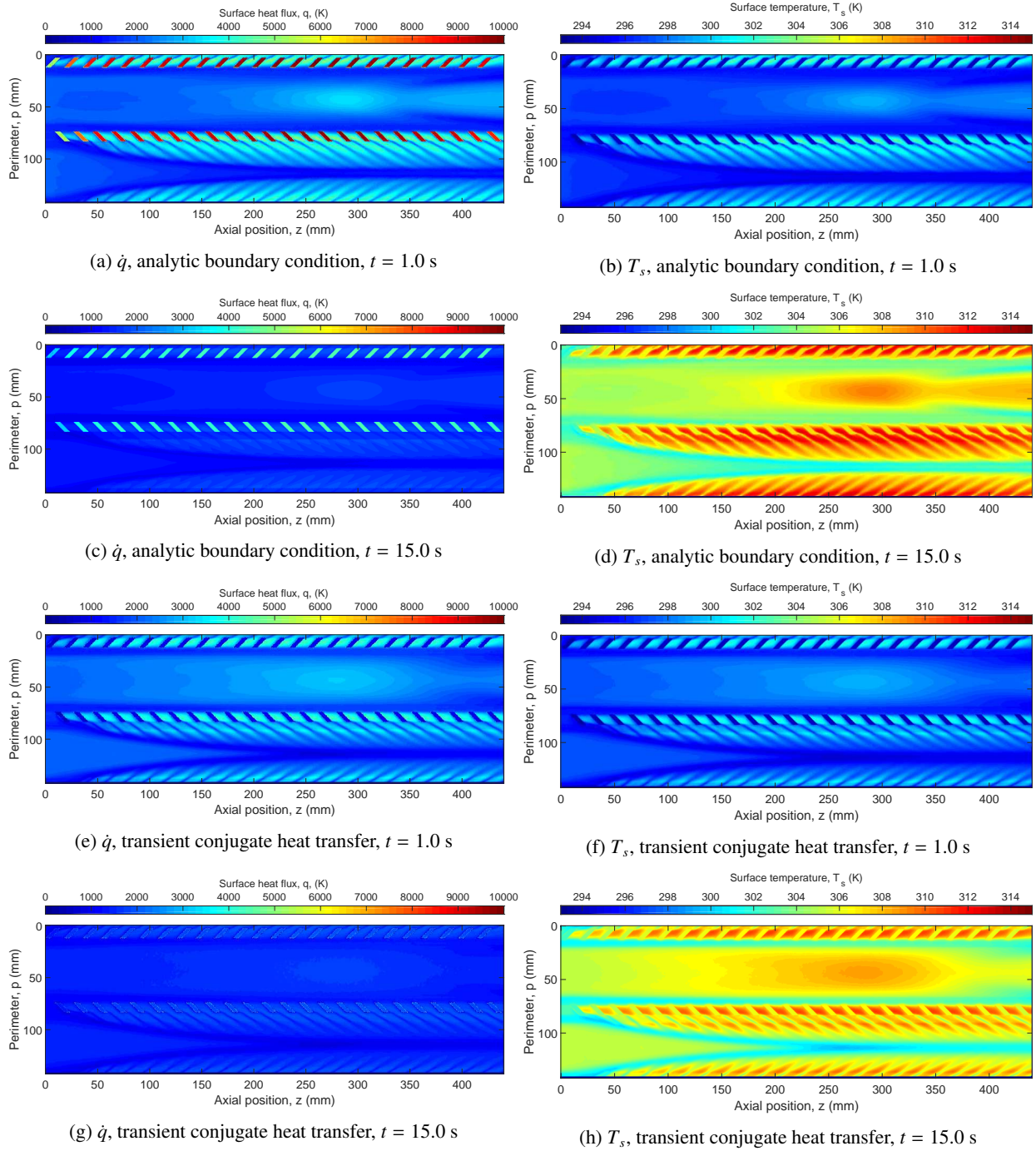


Figure 6: Changing heat flux \dot{q} and surface temperature T_s from analytic boundary condition and transient conjugate heat transfer simulations. Left column: surface heat flux. Right column: surface temperature.

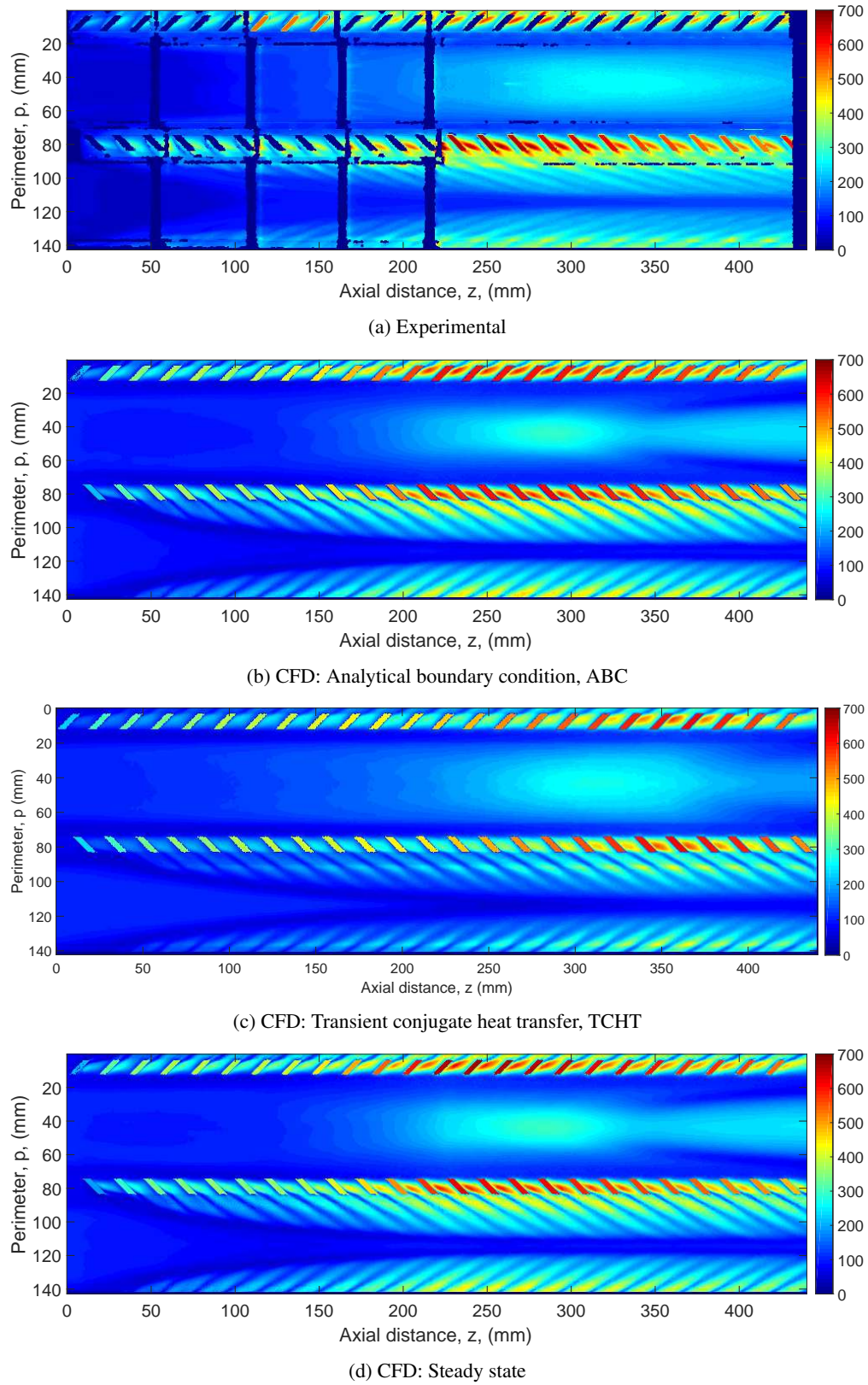
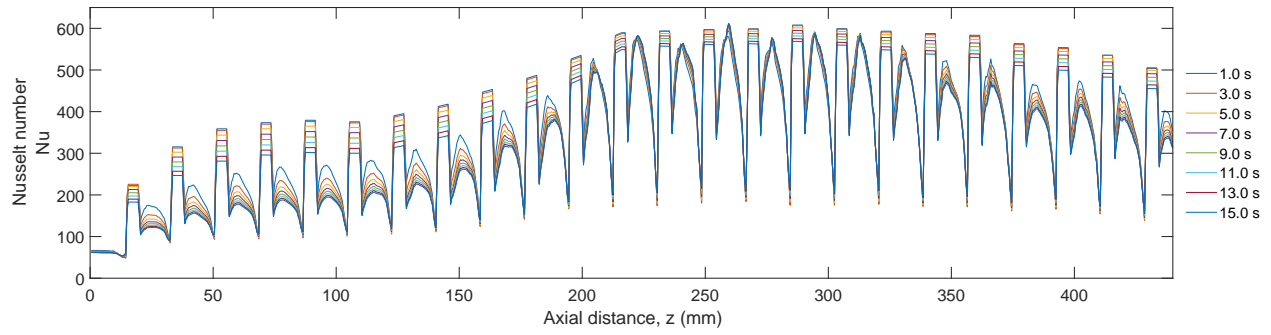
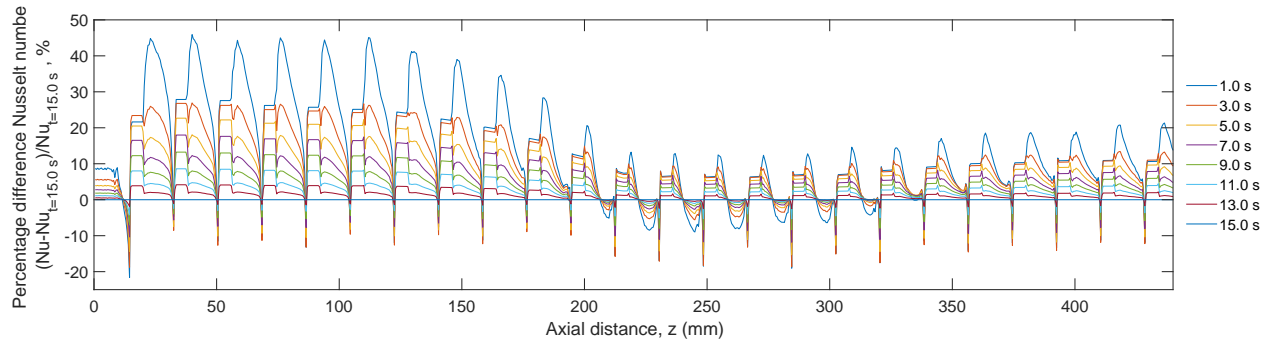


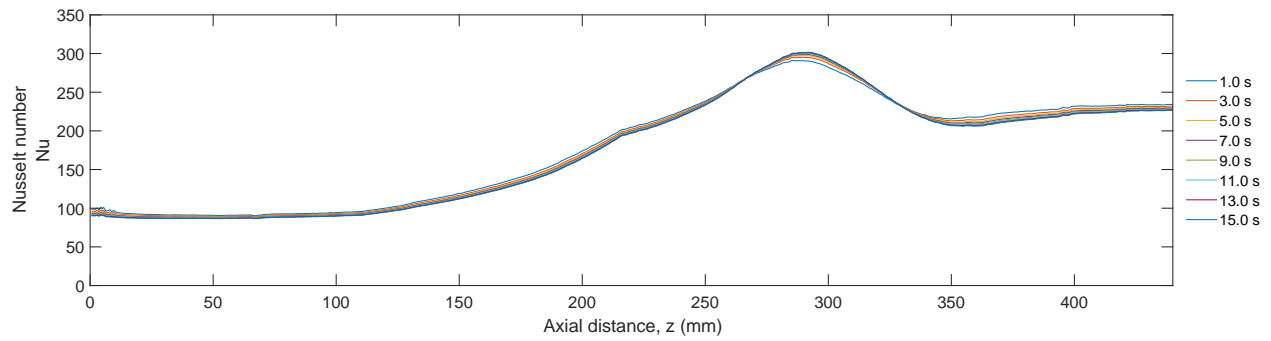
Figure 7: Nusselt number distributions for experiment, analytic boundary condition, transient conjugate heat transfer, and steady state simulations. $Re = 60\,000$, turbulence model $k - \omega$ SST.



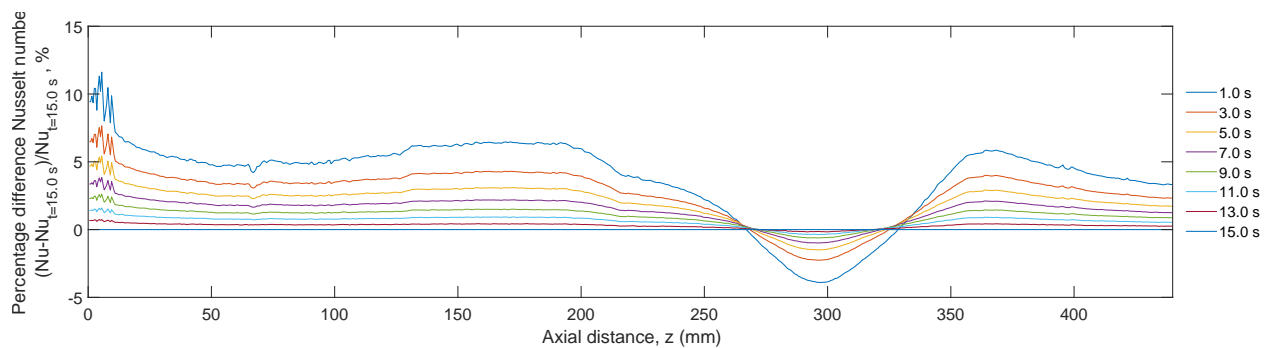
(a) Mid-pressure side



(b) Mid-pressure side, normalised against $Nu_{t=15.0 \text{ s}}$



(c) Mid-trailing edge



(d) Mid-trailing edge, normalised against $Nu_{t=15.0 \text{ s}}$

Figure 8: Variation and percentage difference of Nusselt number with time for (a,b) mid-pressure side ($p = 80\text{mm}$), and (c,d) mid-trailing edge ($p = 45 \text{ mm}$)

3. Fully transient

A fully-transient analytical boundary condition case was run for comparison to the quasi-transient approach. This was also run using ANSYS Fluent 18.2, with a fixed time step equal to $1/10^{\text{th}}$ the ABC time step. The ABC time step was maintained at 0.025 s. A maximum of 30 inner iterations per time step were allowed.

In comparison to the quasi-transient ABC case, the fully transient ABC case showed a slight improvement in pixel-wise mean absolute difference to experimental at 21.4% , and also in area-averaged Nusselt number, at 7.3% below experimental. Rib mean levels were within 1.1% between transient and quasi-transient cases. On the pressure surface and leading edge the transient simulation was 7.2% and 40.0% respectively closer to the experimental values than the quasi-transient, however on the trailing edge the quasi-transient was seen to be 1.3% closer to experimental on average.

Analysis of the fully transient case suggests that the differences between simulation and experimental Nusselt number distributions are not significantly reduced by running fully transient simulations. Further investigation into turbulence modelling are required.

4. Reynolds number

Further simulations were carried out at $Re = 19,000$, $107,000$ for the same aspect ratio passage using the quasi-transient ABC and steady state methods. The same inlet temperature profile was used. The area-averaged normalised Nusselt numbers are shown in Figure 9 for the trailing and leading edges, and pressure surface. Averaging is carried out over the downstream half of the passage.

On the trailing edge the steady state simulations are seen to reproduce the experimental results more closely at all three Reynolds number cases. A maximum disparity of 27.4% is seen for quasi-transient ABC method, and 21.2% for the steady state, both at $Re = 19,000$. The two methods are seen to converge with increasing Reynolds number.

On the leading edge the performance of the two calculation methods is more similar than on the trailing edge. Maximum differences of 10.8% and 15.1% are seen for the ABC and steady state methods respectively. Qualitatively the steady state simulations reproduce the trend seen experimentally with greater fidelity.

On the pressure side the ABC method reproduced the experimental values more closely, though the performance of the methods is quantitatively similar: absolute differences for the ABC method range 10.6-13.3%, and 10.6-17.3% for the steady state simulations. Neither method well-captures the qualitative trend of decreasing normalised Nusselt number with increasing Reynolds number.

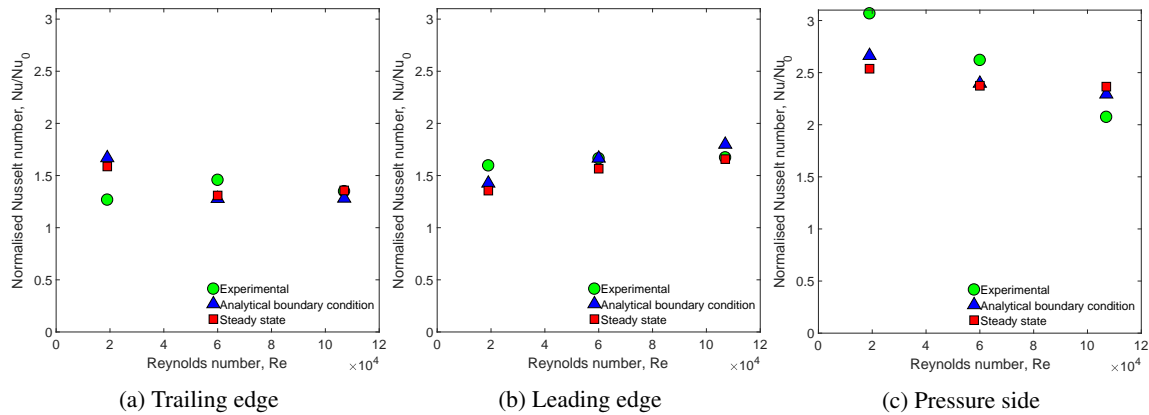


Figure 9: Area-averaged normalised Nusselt number. Normalisation done by smooth pipe Nusselt number correlation (Eq. 2).

V. Summary

A new method for the direct simulation of transient thermochromic liquid crystal experiments has been implemented. On an iterative basis the surface heat flux from steady state simulations is used to calculate the surface temperature response as a series of impulse responses. The new surface temperature is then applied as a boundary condition to the simulation and the fluid re-solved. A transient inlet temperature profile was applied. This quasi-transient analytical boundary condition method is able to capture the changing streamwise gas temperature profile with time, as seen

experimentally, which was thought to be a key driver for the disparity between previous steady state simulations and experiments.

Simulations carried out using the ABC and steady state methods indicated that the two methods performed very similarly across the range of conditions undertaken. Going to a fully transient ABC method was shown to produce small improvements in the matching to experimental data. Simulations undertaken using transient conjugate heat transfer showed greater differences in pixel-wise Nusselt number distribution and area averaged in comparison to the experimental data than the ABC or steady state methods, thought to be due to differences in centreline gas temperature.

Transient variation of the Nusselt number distributions were noted at some locations. In the early stages of the simulations, $t \leq 1.0$ s, these variations were up to 40% relative to the end value ($t = 15.0$ s) in the developing flow region. The variation was seen to quickly reduce with increasing simulation time. Away from the ribbed walls the transient differences in Nusselt number were seen to be small ($< 5\%$).

Further development of the method will include expanding the range of turbulence modelling applied, and investigations into the root causes of the transient behaviour noted of heat transfer coefficient/Nusselt number distributions.

Acknowledgements

This research could not have been undertaken without the support of Christian Orozco-Pineiro and his insightful discussions throughout the EU-funded ERICKA programme.

References

- [1] Shultz, D. L. and Jones, T. V., "Heat transfer measurements in short-duration hypersonic test facilities," AGARDograph 165, 1973.
- [2] Ireland, P. T. and Jones, T. V., "Liquid crystal measurements of heat transfer and surface shear stress," *Measurement Science Technology*, 2000, pp. 969–986.
- [3] Oldfield, M. L. G., "Impulse Response Processing of Transient Heat Transfer Signals," *ASME Journal of Turbomachinery*, Vol. 130, April 2008.
- [4] Buttsworth, D. R. and Jones, T. V., "Technical note: Radial conduction effects in transient heat transfer experiments," *Aeronautical Journal*, Vol. 101, No. 1005, 1997, pp. 209–212.
- [5] Ling, J. P., Ireland, P. T., and Turner, L., "A Technique for processing transient heat transfer, liquid crystal experiment in the presence of lateral conduction," ASME Turbo Expo, Paper GT2003-38446, 2003.
- [6] Coletti, F., Scialanga, M., and Arts, T., "Experimental investigation of conjugate heat transfer in a ribroughened trailing edge channel with crossing jets," ASME Turbo Expo, Paper GT2010-22432, 2010.
- [7] Ryley, J. C., McGilvray, M., and Gillespie, D. R. H., "Calculation of Heat Transfer Coefficient Distribution on 3D Geometries From Transient Liquid Crystal Experiments," ASME Turbo Expo, Paper GT2014-26973, 2014.
- [8] Forsyth, P., McGilvray, M., and Gillespie, D. R. H., "Secondary flow and heat transfer coefficient distributions in the developing flow region of ribbed turbine blade cooling passage," *Experimental Fluids*, Vol. 58, No. 5, 2017.
- [9] O'Dowd, D., Znag, Q., He, L., Ligrani, P., and Friedrichs, S., "Comparison of Heat Transfer Measurement Techniques on a Transonic Turbine Blade Tip," *Journal of Turbomachinery*, Vol. 133, 2011.
- [10] Gillespie, D., *Intricate Internal Cooling Systems for Gas Turbine Blading*, DPhil thesis, University of Oxford, 1996.
- [11] Camci, C., Kim, K., and Hippensteele, S., "A new hue capturing technique for quantitative interpretation of liquid crystal images used in convective heat transfer studies," *Journal of Turbomachinery*, Vol. 114, 1992, pp. 765–775.
- [12] Ireland, P., Neely, A., Gillespie, D., and Robertson, A., "Turbulent heat transfer measurements using liquid crystals," *International Journal of Heat and Fluid Flow*, Vol. 20, No. 4, 1999, pp. 355–367.
- [13] Cukurel, B. and Arts, T., "Local Heat Transfer Dependency on Thermal Boundary Condition in Ribbed Cooling Channel Geometries," *Journal of Heat Transfer*, Vol. 135, 2013.
- [14] Maffulli, R. and He, L., "Impact of Wall Temperature on Heat Transfer Coefficient and Aerodynamics for Three-Dimensional Turbine Blade Passage," *Journal of Thermal Science Engineering and Applications*, Vol. 9, No. 4, 2017.
- [15] Sathyanarayanan, S. and Shih, T.-P., "Time-Accurate Conjugate Analysis of Transient Measurements of Heat Transfer Coefficients," *Journal of Thermophysics and Heat Transfer*, Vol. 31, No. 3, 2017, pp. 527–537.
- [16] Ryley, J., McGilvray, M., and Gillespie, D. R. H., "Stationary Internal Cooling Passage Experiments for an Engine Realistic Configuration," 10th European Conference on Turbomachinery, Fluid Dynamics and Thermodynamics, 2013.
- [17] McGilvray, M., Orozco Pieiro, C., Axe, T., Ryley, J., and Gillespie, D. R. H., "Comparison of Stationary Internal Cooling Passage Experimental Data to Numerical Simulations," 10th European Conference on Turbomachinery, Fluid Dynamics and Thermodynamics, 2013.

- [18] McGilvray, M., Ryley, J., and Gillespie, D. R. H., "Investigation of wrapping ribs onto smooth walls for mid-chord internal cooling passages," ASME Turbo Expo, Paper GT2014-26800, 2014.
- [19] He, L. and Oldfield, M. L. G., "Unsteady Conjugate Heat Transfer Modelling," *Journal of Turbomachinery*, Vol. 133, July 2011.
- [20] Wang, Z., "The Application of Thermochromic Liquid Crystals to Detailed Turbine Blade Cooling Measurements," D. Phil. Thesis, University of Oxford, 1991.